ELSEVIER

Volume 183, Issue 4, April 2010

JOURNAL OF SOLID STATE CHEMISTRY

www.elsevier.com/locate/jssc

CONTENTS

Abstracted/indexed in BioEngineering Abstracts, Chemical Abstracts, Coal Abstracts, Current Contents/Physics, Chemical, & Earth Sciences, Engineering Index, Research Alert, SCISEARCH, Science Abstracts, and Science Citation Index. Also covered in the abstract and citation database SCOPUS®. Full text available on ScienceDirect®.

Regular Articles

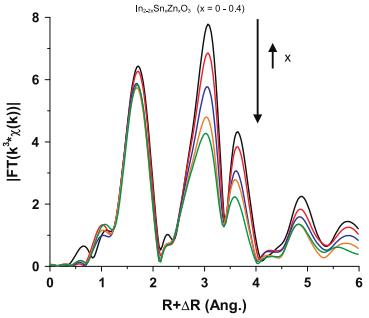

The local structure of Zn and Sn cosubstituted In_2O_3 was determined by X-ray absorption spectroscopy, which was consistent with random substitutions of In by Zn and Sn into bixbyite In_2O_3.

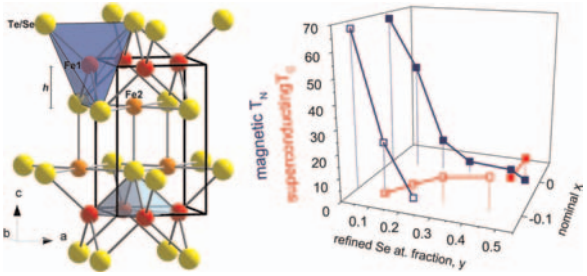

Single crystals of $Fe_{1+x}Te_{1-y}Se_y$ have been grown with a controlled Fe off-stoichiometry and Se doping and the crystal structure has been refined for various compositions, thus proving the effect of both Fe excess and Se-substitutions on the structural properties. Either antiferromagnetic or superconducting ground state is driven by doping and related structural modifications. An improved 3-D phase diagram is proposed.

Regular Articles—Continued

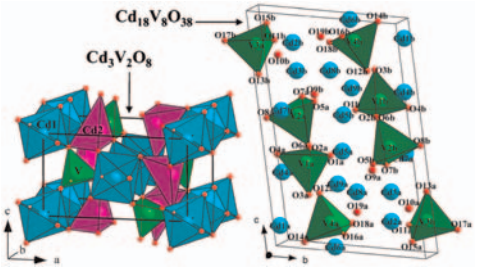

The binary compounds $Cd_3V_2O_8$ and $Cd_{18}V_8O_{38}$ have been successfully synthesized by solid state reaction route and the crystal structures were determined from single-crystal X-ray diffraction data.

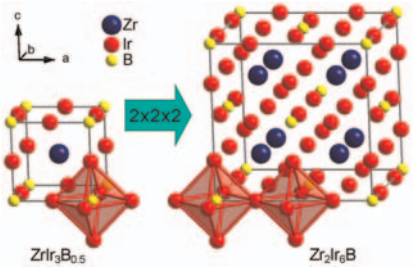

Zr_2Ir_6B crystallizes with an eightfold superstructure of the already reported simple cubic perovskite $ZrIr_3B_x$. According to the result of tight-binding electronic structure calculations, Ir–B and Ir–Zr interactions are mainly responsible for its structural stability, and the Ir–Ir bonding within the empty Ir_6 clusters is two times stronger than that in the BIr_6 octahedra.

Continued

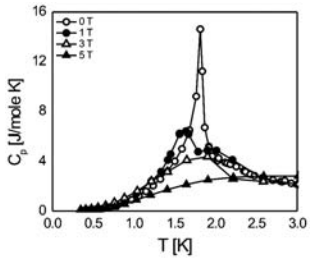

Low-temperature specific heat of $NdAg_2Ge_2$ under external magnetic fields. The λ-like anomaly originates from onset of magnetic ordering below 1.80 K. Shifting the anomaly position towards the lower temperatures, when raising the magnetic field, hints at antiferromagnetic behaviors.

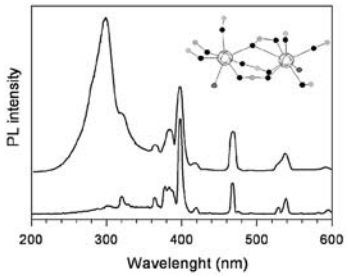

Excitation spectra monitoring the $^5D_0 \rightarrow {}^7F_2$ transition with a dimer structure.

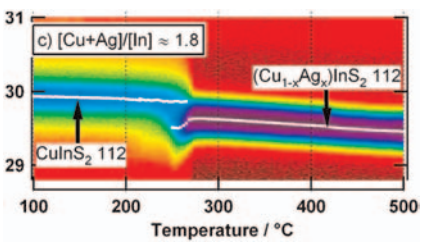

In-situ monitoring by means of energy-dispersive X-ray diffraction of the thin-film recrystallization of Cu-poor $CuInS_2$ assisted by metallic Ag.

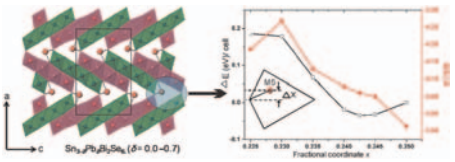

New ternary and quaternary chalcogenides, $Sn_{3-\delta}Pb_\delta Bi_2Se_6$ (δ = 0.0–0.7), were synthesized and their structures are related to that of $Pb_3Bi_2S_6$ with an atomic position near the cell-twinning plane. Band structure calculations confirmed that the structure is stabilized when the position of the $M5$ site is farther from the cell-twinning plane. All compounds are n-type semiconductors with small band gaps.

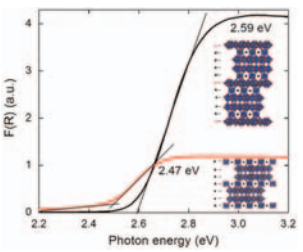

The copper(I) tantalates, $Cu_5Ta_{11}O_{30}$ and $Cu_3Ta_7O_{19}$, were synthesized by high-temperature solid-state reactions and by a new CuCl flux method, respectively. Their structures consist of single and double layers of TaO_7 pentagonal bipyramids separated by isolated TaO_6 octahedra and Cu atoms. UV–vis spectra show visible-light bandgap sizes of $\sim$2.5–2.6 eV, which LMTO calculations show arise primarily from indirect transitions between the filled Cu $3d^{10}$ and the empty Ta $5d^0$ orbitals in the TaO_7 pentagonal bipyramids.

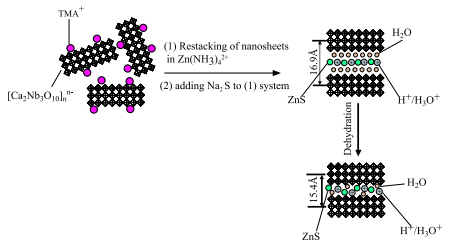

ZnS/niobate composites were first synthesized by exfoliation/self-assembly processing. The composites were characterized by X-ray diffraction (XRD), high-resolution transmission electron microscopy (HRTEM), X-ray photoelectron spectroscopy (XPS), scanning electron microscope (SEM) and energy dispersive spectrometer (EDS), IR spectrum, UV-vis spectrum, and photoluminescent spectrum. The photoluminescence spectrum of the ZnS/niobate composite shows blue shift attributed to quantum sizes effects.

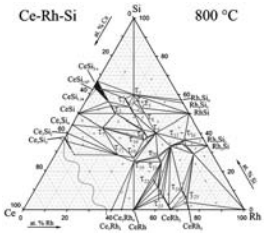

Phase relations in the ternary system Ce–Rh–Si have been established for the isothermal section at 800 °C based on X-ray powder and single-crystal diffraction, metallography, SEM and EMPA techniques on about 80 alloys. 25 ternary compounds were observed.

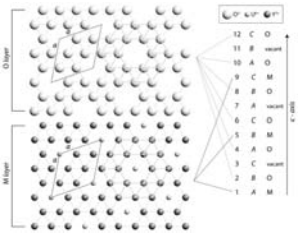

The different order-to-disorder (O–D) phase transformation tendencies in irradiated uranium-bearing δ-phase $RE_6U_1O_{12}$ compounds ($Y_6U_1O_{12}$, $Gd_6U_1O_{12}$, $Ho_6U_1O_{12}$, $Yb_6U_1O_{12}$, and $Lu_6U_1O_{12}$) are revealed by grazing incidence X-ray diffraction and transmission electron microscopy measurements, and theoretical simulations of the O–D transformation energies, performed using DFT, also support our experimental results.

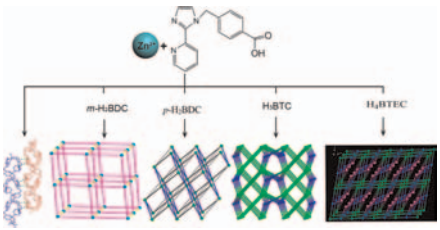

Five novel Zn^{II}-organic architectures have been hydrothermally synthesized through varying auxiliary aromatic-acid ligands and characterized by X-ray diffraction, the photoluminescence properties of compounds **1–5** were studied.

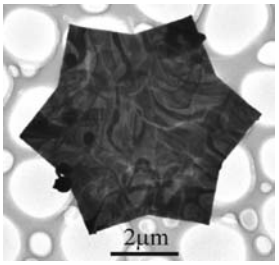

If a temperature difference was introduced to the gel of $Au^{3+}(H_2O)$-PVP, large sized Au nanoplates with new and well-defined star shape were observed.

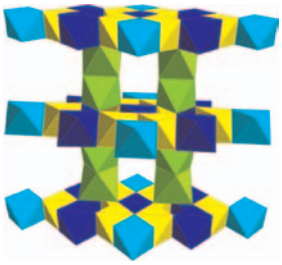

A complete solid solution is formed between isostructural $Pb_3Mn_7O_{15}$ and $Pb_3Rh_7O_{15}$. The effect of Mn substitution for Rh on the previously discovered Verwey-type transition in $Pb_3Rh_7O_{15}$ is described.

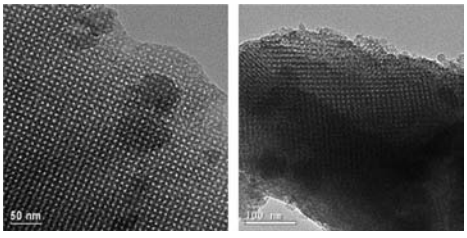

Novel organic–inorganic mesoporous luminescent hybrids containing RE^{3+} complex covalently attached to the β-diketone-functionalized ordered mesoporous SBA-16, which were designated as bpy-*RE*-TTA-S16 and bpy-*RE*-DBM-S16, were obtained by sol–gel process.

Continued

Ferromagnetic ordering in $ThSi_2$ type $CeAu_{0.28}Ge_{1.72}$
C. Peter Sebastian and Mercouri G. Kanatzidis
Page 878

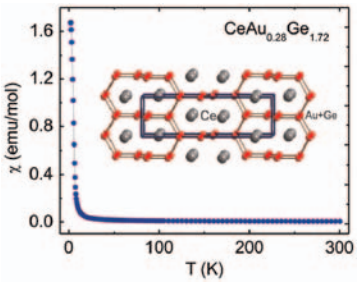

$CeAu_{0.28}Ge_{1.72}$ crystallizes in the $ThSi_2$ structure type in the tetragonal space group $I4_1/amd$ and orders ferromagnetically at ~ 8 K.

Morphological and structural evolution of α-MnO_2 nanorods synthesized via an aqueous route through MnO_4^-/Mn^{2+} reaction
Xiaobo Fu, Jiyun Feng, Huan Wang and Ka Ming Ng
Page 883

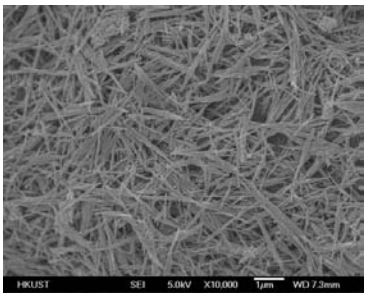

α-MnO_2 nanorods were synthesized via an aqueous route through MnO_4^-/Mn^{2+} reaction under mild conditions.

Spin glass transitions in the absence of chemical disorder for the pyrochlores $A_2Sb_2O_7$ (A = Mn, Co, Ni)
H.D. Zhou, C.R. Wiebe, J.A. Janik, B. Vogt, A. Harter, N.S. Dalal and J.S. Gardner
Page 890

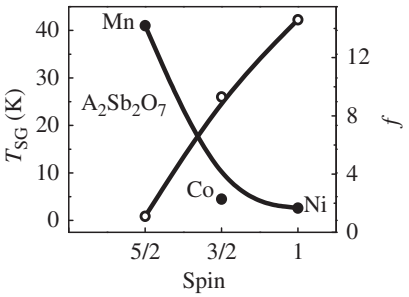

A comparison of the spin glass ordering temperature, T_{SG}, and the frustration index f as a function of the spin for the pyrochlore series $A_2Sb_2O_7$. In the limit of low spin, the frustration index increases by an order of magnitude.

Structural phase transition and 5*f*-electrons localization of PuSe explored by *ab initio* calculations
Shouxin Cui, Wenxia Feng, Haiquan Hu, Zizheng Gong and Hong Liu
Page 895

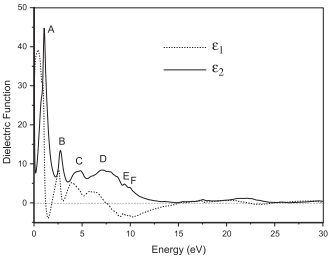

5*f*-electrons are more localized by the analysis of the density of states (SOC). The origin spectra peaks was interpreted based on electronic structures.

Experimental and *ab initio* infrared study of χ-, κ- and α-aluminas formed from gibbsite
L. Favaro, A. Boumaza, P. Roy, J. Lédion, G. Sattonnay, J.B. Brubach, A.M. Huntz and R. Tétot
Page 901

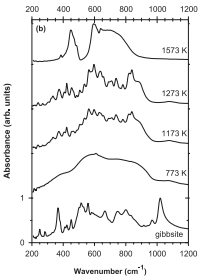

Infrared spectra of the sequence Gibbsite $\rightarrow\chi\rightarrow\kappa\rightarrow\alpha$-$Al_2O_3$ obtained from 24 h calcinations of Gibbsite at 773 K, 1173 K, 1273 K and 1573 K. All intensity maxima are normalized at 1.

Origin of periodic domain structure in Er^{3+}-doped β′-$(Sm,Gd)_2(MoO_4)_3$ crystal lines patterned by laser irradiations in glasses
Futoshi Suzuki, Tsuyoshi Honma and Takayuki Komatsu
Page 909

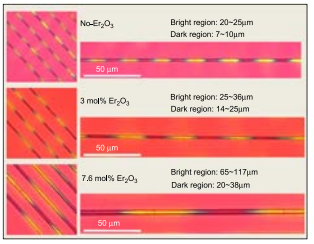

This figure shows the polarized optical photographs (top view) for the lines patterned by laser irradiations with the power of $P = 1.3$ W and the scanning speed of $S = 5$ μm/s in xEr_2O_3–$(18.25-x)Gd_2O_3$–$3Sm_2O_3$–$63.75MoO_3$–$15B_2O_3$ (mol%) glasses. This figure indicates that the periodicity of domain structures in β′-$(Sm,Gd)_2(MoO_4)_3$ crystal lines, i.e., the lengths of bright (high refractive index) and dark (low refractive index) color regions, changes depending on the amount of Er_2O_3 addition. It is demonstrated that the origin of the periodicity of domain structures is due to spontaneous strains in ferroelastic β′-$(Sm,Gd)_2(MoO_4)_3$ crystals.

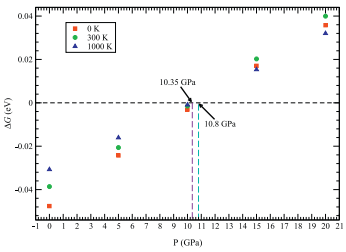

Pressure induced structural phase transition from the orthorhombic structure to the hexagonal one for OsB_2 takes place under 10.8 GPa (0 K), 10.35 GPa (300, 1000 K) by the first-principles predictions.

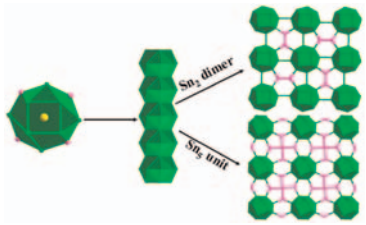

Two new ytterbium nickel stannides, namely, $Yb_5Ni_4Sn_{10}$ and $Yb_7Ni_4Sn_{13}$, have been synthesized and structurally characterized by single-crystal X-ray diffraction studies. Both their structures feature three-dimensional (3D) frameworks based on three different types of one-dimensional (1D) channels, which are situated by all the Yb atoms. Electronic structure calculations based on density functional theory (DFT) indicate that both compounds are metallic, which are in accordance with the results from temperature-dependent resistivity and magnetic susceptibility measurements.

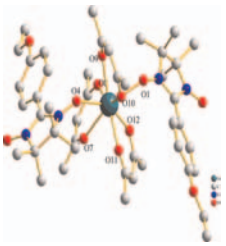

Two tri-spin complexes based on gadolinium-radical have been synthesized and characterized, the magnetic studies show that in the two complexes the Gd–radical interaction is ferromagnetic and the radical–radical interaction is antiferromagnetic. An analogous complex containing the diamagnetic Lu^{III} ions has also been synthesized to further demonstrate the nature of the magnetic coupling between radicals.

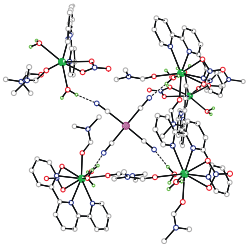

The synthesis of an isostructural series of lanthanide tetracyanoplatinates incorporating 2,2′:6′,2″-terpyridine are presented. Solid-state absorption and luminescence properties are discussed for the Eu^{3+} and La^{3+} compounds.

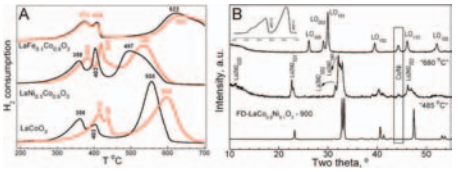

$LaCo_{1-x}Ni_xO_3$ and $LaCo_{1-x}Fe_xO_3$ with rhombohedrally distorted perovskite structure were obtained in the temperature range of 600–900 °C by thermal decomposition of freeze-dried La–Co/Ni(Fe)-citrates and by the Pechini method. The complete reduction of $LaCo_{1-x}Ni_xO_3$ with H_2 proceeds to Co/Ni-metal and La_2O_3, while the interaction of $LaCo_{1-x}Fe_xO_3$ with H_2 is not complete up to 700 °C. For $LaCo_{1-x}Fe_xO_3$, the reaction proceeds by preferential oxidation of Co^{3+} to Co^{2+} without affecting Fe^{3+} ions.

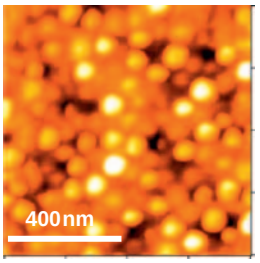

AFM surface image of the emulsion particles with the spin crossover complex.

Continued

Synthesis of hydrophobic zinc borate nanoflakes and its effect on flame retardant properties of polyethylene
Shengli Li, Beihong Long, Zichen Wang, Yumei Tian, Yunhui Zheng and Qian Zhang
Page 957

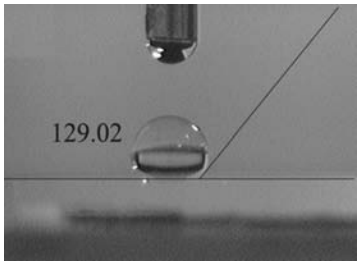

The contact angle of hydrophobic zinc borate nanoflakes is 129.02° with added 2.0 wt% of oleic acid.

Morphological development and oxidation mechanisms of aluminum nitride whiskers
Xin-mei Hou, Chang-sheng Yue, Ankit Kumar Singh, Mei Zhang and Kuo-Chih Chou
Page 963

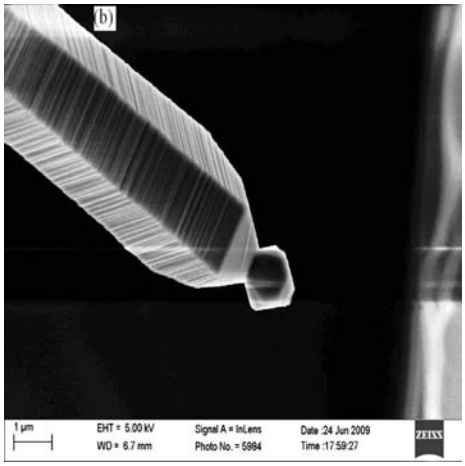

Hexagonal aluminum nitride (AlN) whiskers have been synthesized at 1873 K under a flowing nitrogen atmosphere. The synthesized whiskers are long straight filaments with diameters between 1 and 5 μm and length in the cm range.

Carbon/λ-MnO_2 composites for supercapacitor electrodes
A. Malak-Polaczyk, C. Matei-Ghimbeu, C. Vix-Guterl and E. Frackowiak
Page 969

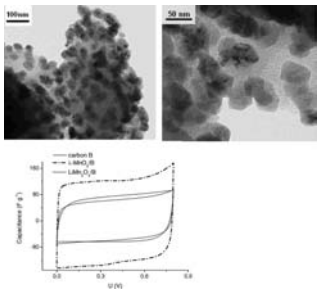

Comparison of capacitance characteristics for initial carbon and synthesised composites for CB in 1 mol L^{-1} Na_2SO_4 solution.